Hydrothermal Steel Slag Valorization—Part II: Hydrogen and Nano-Magnetite Production

Camille Crouzet [1,2,3], Fabrice Brunet [1*], Nadir Recham [2,4], Anne-Line Auzende [1], Nathaniel Findling [1], Valérie Magnin [1], Jean-Henry Ferrasse [3] and Bruno Goffé [5]

[1] Univ. Grenoble Alpes, Univ. Savoie Mont Blanc, CNRS, IRD, IFSTTAR, ISTerre, Grenoble, France, [2] LRCS, CNRS-UMR7314, Univ. Picardie Jules Verne, Amiens, France, [3] Aix Marseille Univ., CNRS, Centrale Marseille, M2P2, Marseille, France, [4] RS2E, FR CNRS 3459, Univ. Picardie Jules Verne, Amiens, France, [5] Aix-Marseille Univ., CNRS, IRD, Collège de France, CEREGE, Aix en Provence, France

The effect of acidic conditions (in a pH range of 3 to 6) and temperature on the kinetics of the hydrothermal oxidation of ferrous iron contained in BOF steel slag has been tested in the 150–350°C range for acid acetic concentrations from 0 to 4 M. Reaction progress was monitored with the amount of produced H_2. Higher temperature and lower pH are found to enhance the hydrothermal oxidation kinetics of the slag. These two parameters are believed to increase iron dissolution rate which has already been identified as the rate limiting step of the hydrothermal oxidation of pure FeO. An activation energy of 28 $\pm$ 4 kJ/mole is found for the hydrothermal oxidation of the steel slag which compares very well with that of pure FeO under similar conditions. In the case of the slag run in water at 300°C for 70.5 h, magnetite product has been separated magnetically and characterized. Particles were found to fall in three size ranges: 10–30 nm, 100–300 nm, and 1–10 μm. The smallest fraction (10–30 nm) is comparable to the 10–20 nm size range that is achieved when nanomagnetite are synthesized by co-precipitation methods. Obviously, the production of nanomagnetite enhances the economic interest of the hydrothermal processing of steel slags, which has already proven its capacity to produce high-purity H_2.

Keywords: magnetite, nanoparticles, BOF steel slag, hydrothermal oxidation, hydrogen production

INTRODUCTION

The context of a rising demand in energy and in raw materials, with the constraint of restraining our impact on the environment, is a driver for finding alternative energy and material resources in the frame of a circular economy. In this context, Malvoisin et al. (2013) proposed to recover part of the steelmaking energy stored chemically in steel slags using a novel process which produces high-purity hydrogen through the hydrothermal oxidation of steel slags. This process is inspired from the abiogenic geochemical process of native dihydrogen (H_2) formation operating at mid-oceanic ridges (Charlou et al., 2002; Marcaillou et al., 2011). Under these hydrothermal conditions (350°C—500 bar), ferrous iron-bearing magnesium silicates are hydrated and oxidized by hot seawater. Ferrous iron is partly incorporated as ferric iron in $Fe^{2+}Fe_2^{3+}O_4$ magnetite whereas the reduction of water leads to the formation of H_2. Applied to low value Fe^{2+}-bearing wastes such as steel slags, high-purity hydrogen can be produced at a limited cost. Developed in the beginning

of the twentieth century, the first industrial method for producing high purity hydrogen—named steam-iron process—was based on the same principle (Hacker et al., 2000; Lorente et al., 2011). Hydrogen was produced through cycles of iron metal oxidation by steam and iron oxide reduction by gasified coal at temperatures ranging from 550 to 900°C. However, even if promising hydrogen technologies such as fuel cells are under a growing interest, the hydrogen market struggles to expand and to diversify its production sources. Hydrogen remains nowadays mainly produced from fossil fuels at a very low cost but with significant CO$_2$ emissions.

In other words, today, the value of hydrogen alone is not sufficient to stimulate the required investments to develop hydrothermal processing of byproducts or waste at an industrial scale. However, in addition to high-purity hydrogen production, hydrothermal oxidation of steel slag leads to the formation of magnetite particles. Fine magnetite particles (<1 mm) are for example used to produce radiation shielding concretes (Creutz and Downes, 1949), pigments (Legodi and Dewaal, 2007), catalysts (Gawande et al., 2013; Munoz et al., 2015), or dense materials such as ballast (Ahles, 1946). The production of toner for printers requires a narrow particle size distribution of hundred nanometers (Sacripante and Kmiecik-Lawrynowicz, 1994; Patel et al., 2003) whereas smaller particles are required for an use as contrast agents for medical imaging (Tiefenauer et al., 1996; Mornet et al., 2004; Morawski et al., 2005). Ferrofluids which exhibit magnetic dependent rheology properties and high heat-transfer capacities are made of magnetite nanoparticles (Kim et al., 2005; Drozdov et al., 2016). Ferrofluids have been used for years as automobile dampers, hard disk seals or in dynamic loudspeakers (Raj and Moskowitz, 1990; Raj et al., 1995). In recent years, research on nano-magnetite applications focused on wastewater treatment. For example, the possibility of magnetic recovery coupled with high reactive surface area opens promising applications for the remediation of waters polluted with heavy metals (Hua et al., 2012; Xu et al., 2012). Keeping in mind that magnetite can be recovered from its matrix using magnetic-based separation methods, the hydrothermal treatment of iron-bearing byproducts may gain additional value with the production/separation of magnetite.

We have shown by using reagent grade FeO taken as an analog of Mg-bearing wüstite contained in slags, that the dissolution of ferrous iron is the rate limiting step to H$_2$ production/nano-magnetite formation (Crouzet et al., 2017). This latter study allowed to highlight the strong positive effect of mild acetic acid on the overall FeO oxidation kinetics. As an example, an acetic acid concentration of 0.05 M and a temperature of 150°C were sufficient to reach 87% of reaction progress within 10 h of experiment. However, Crouzet et al. (2017) showed that the beneficial effect of adding a mild acidic solution onto pure FeO does not directly transpose to steel slags which are strongly alkaline owing to a high CaO content (>40 wt.%). Crouzet et al. (in press) actually proposed to neutralize that free CaO with carbonic acid by carbonating the steel slag prior and during the oxidation step.

Here, in order to achieve Ca-rich steel slag oxidation under acidic hydrothermal conditions, we explored two oxidation routes: (1) hydrothermal oxidation with concentrated acetic acid and (2) hydrothermal oxidation in the presence of mild acetic acid after the cold removal of calcium.

MATERIALS AND METHODS

Starting Materials

A basic oxygen furnace (BOF) steel slag sample with only a few weeks of outdoor storage was selected for this study. The corresponding chemistry and mineralogy are described in Crouzet et al. (in press). Prior to its hydrothermal treatment, the starting slag was crushed down to an average particle size of 20 μm. Another starting material was prepared from the crushed slag by removing calcium with acetic acid which is known for its ability to efficiently dissolve calcite, portlandite and larnite at room temperature (Kakizawa et al., 2001). About 10 g of steel slag were added to 500 ml of a 4 M acetic acid solution under magnetic stirring. After 1 h, the solid residue was rinsed with de-ionized water and filtered through a 0.45 μm porous nitrocellulose membrane. Recovered solid was finally dried at 80°C for about 12 h.

Hydrothermal Oxidation

Sampling Autoclave: Hydrogen Production and Ferrous Iron Dissolution Monitoring

Hydrothermal oxidation of the ferrous iron contained in the steel slag (Equation 1) by liquid water leads to the formation of hydrogen and magnetite (Malvoisin et al., 2013). This reaction was investigated in a 500 ml autoclave equipped with gas and solution sampling capillaries (see Crouzet et al., 2017). From 2 to 20 g of steel slag are inserted in 200 ml of either de-ionized water or 1 M acetic acid solution (starting pH of 2.5). The autoclave is heated by two external collars. Temperatures in the 250–350°C range were investigated. An initial pressure of 50–100 bar of argon (Ar) was set at ambient temperature to reach 180–230 bar at the temperature set-point. The slag suspension is stirred at a rotation speed of 500 rpm. H$_2$ production will be expressed hereafter as the mass of H$_2$ divided by the equivalent FeO mass content of steel slag. Potentially, up to 9.28 g H$_2$ per kg FeO can be produced according to the following reaction:

$$3FeO_{(s)} + H_2O_{(l)} \rightarrow Fe_3O_{4(s)} + H_2 \qquad (1)$$
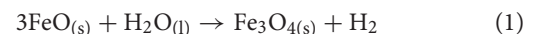
The sampled gas is injected into a gas chromatograph (Clarus 500 GC, Perkin Elmer) run under a constant argon gas flow of 30 mL/min; the gas components (H$_2$, CO$_2$, N$_2$, O$_2$, CO, CH$_4$) are separated with a polymer filled column (Restek ShinCarbon®). Chemical identification and quantification were performed by comparing retention times with a reference gas mixture using a thermal conductivity detector (TCD). The temperature of the detector, the injection system and the oven were respectively set to 250, 100, and 80°C. The determination of the produced H$_2$ mass which involves sampling and GC measurement is believed to be accurate to ±10%.

Aliquots of 2 ml aqueous solution were sampled with a plunging capillary and collected in a 20 ml syringe after filtering through a 0.45 μm porous nitrocellulose membrane. Iron content

TABLE 1 | Semi-quantitative μXRF analysis (error ± 20%) of the three steel slag samples, i.e., starting slag, de-calcified slag, and the recovered sample after oxidation of the decalcified slag (*APAc-1M-250C*).

wt.%	MgO	Al$_2$O$_3$	SiO$_2$	P$_2$O$_5$	SO$_3$	CaO	TiO$_2$	V$_2$O$_5$	Cr$_2$O$_3$	MnO	FeO	NiO	CuO	LOI
Starting	5.0	1.5	13.6	5.3	0.4	45.2	0.3	0.1	0.2	2.1	18.5	*bdl*	*bdl*	8.3
After Ca removal	10.4	4.3	9.1	9.6	0.2	18.3	0.9	0.2	0.3[a]	3.2	39.8	*bdl*[a]	*bdl*	3.7
After oxidation	1.8	6.8	7.2	9.4	2.7	5.4	1.8	0.3	2.9[a]	1.1	47.6	9.1[a]	0.3	3.7

[a]*Increase in Ni and Cr, before and after oxidation, is interpreted as contamination from the Hastelloy reactor.*

was then determined by UV-spectroscopy after complexation by orthophenantroline. This method allowed a fast quantification with a detection limit of 0.1 ppm and an estimated error of 10%. When lower iron concentrations were expected, total iron content was quantified by ICP-OES. The pH of the recovered aliquot was measured at ambient temperature with pH paper indicators.

Sealed Gold Capsules

The effect of temperature and initial acid acetic concentration on the hydrothermal oxidation of steel slag was first investigated by conducting a set of experiments in 2-cm long gold-capsules. Around 80 mg of steel slag and 80 mg of de-ionized water are loaded in a gold tube (outer diameter of 4.4 mm). The two ends of the tube are welded shut. The encapsulated sample is placed in a cold-seal pressure vessel, itself introduced in a horizontal furnace. Three different initial concentrations of acetic acid, 1, 2, and 4 moles per liter, were investigated at temperatures of 150 and 300°C for a run duration of 3 days. Argon pressure was fixed to 300 bar. The gas entrapped in the capsule was recovered following the method described by Malvoisin et al. (2013) and injected with a 250 μl syringe into a gas chromatograph for analysis.

Magnetic Separation

Magnetite particles produced by hydrothermal oxidation of the steel slag were separated magnetically. After hydrothermal treatment, the solid fraction is recovered and mixed with water in a beaker, itself placed in an ultrasonic bath for at least 20 min. A first separation is achieved by introducing a permanent magnet into the solution. The magnet is either wrapped in a cling film or fitted into a plastic container. After 2 min of immersion, the magnet is taken out and the film (or plastic) cover removed and washed several times in water and ethanol in order to recover the magnetic particles. This extraction process was repeated until no more particles were attracted by the magnet. It appeared that the extracted magnetic particles contained calcium carbonate impurity. Therefore, the magnetic separation procedure described above is repeated by changing water by dilute hydrochloric acid (2 wt.%). After water and ethanol washing, particles were finally dried at ambient temperature in a fume hood.

Solid Phases Characterization

Transmission Electronic Microscopy (TEM) characterization was performed with a Jeol FEG 2100F operated at 200 kV. A drop of the powder sample dispersed in ethanol was deposited on a Lacey carbon-coated grid.

Fast and non-destructive chemical characterization of solid samples was performed on pelletized powders using micro X-ray fluorescence in standard-less mode with no matrix correction (μXRF, EDAX Eagle III). The beam size was set to 300 μm in diameter. The μXRF chemical analysis of the starting steel slag (**Table 1**) was compared to ICP-OES data obtained by Crouzet et al. (in press) on the same material. From this comparison, it appears that μXRF accuracy is better than 20% for all components except SiO$_2$ and P$_2$O$_5$. μXRF analysis was then used to characterize the solid samples retrieved after calcium selective dissolution and the products of hydrothermal oxidation of this secondary starting material.

Additional Field Emission Scanning Electron Microscopy (FE-SEM) observations were conducted along with X-Ray Powder Diffraction (XRPD) using a D8 diffractometer (Bruker, Cu$K\alpha$ radiation) operated with a 2θ step size of 0.026°. Semi-quantitative analysis of crystalline phases was conducted by Rietveld refinement using BMGN software (Taut et al., 1998). The semi-quantitative character of this determination lies in the likely presence of amorphous/poorly crystalline phases and the lack of reliable chemical data for some of the slag-forming minerals. Accuracy in mineral abundances derived from Rietveld cannot be evaluated strictly but absolute errors of ±5–10% may well be encountered. For that reason, instead of providing numbers with no uncertainty, mineral abundances are sorted into three main classes in **Table 2**.
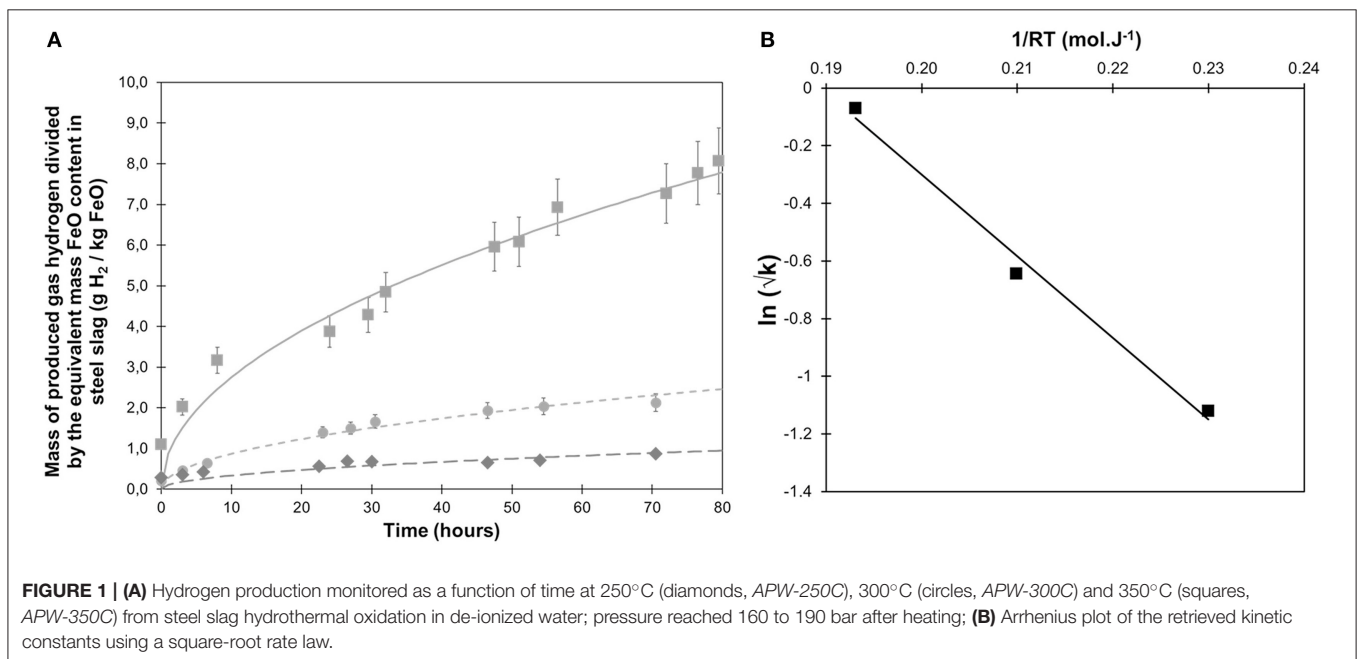
RESULTS

Steel Slag Oxidation in Water
Effect of Temperature

Three experiments were first conducted with steelmaking slag and de-ionized water in a sampling autoclave at 250, 300, and 350°C (**Figure 1A**; *APW-250C*, *APW-300C* & *APW-350C* in **Table 3**). Whatever the investigated temperature, about half of the H$_2$ is produced during the first 24 h. After 24 h and up to the end of the experiment (i.e., 80 h), the H$_2$ production rate slows down and remains roughly constant. Hydrogen production kinetics were all successfully fitted to a square root function of time (Equation 2). A significant dependence in temperature was observed. After 72 h, 0.87, 2.13, and 8.07 g of H$_2$ / kg equivalent FeO were respectively produced at 250, 300, and 350°C. The A_n constant (Equation 2) was estimated to 0.11, 0.28, and 0.87 g H$_2$/h$^{1/2}$/kg FeO at 250, 300, and 350°C, respectively (**Table 3**).

TABLE 2 | Mineralogical phases and relative abundance deduced from semi-quantitative Rietveld refinement Chemical formula is given as a qualitative information except for phases marked with a star (*) for which data were retrieved from initial steel slag characterization (Crouzet et al., in press); +++ dominant, ++ abundant, + minor, (+) trace.

	Starting material*	After oxidation at 300°C in water*	After RT dissolution in acetic acid (4 M)—decalcified steel slag	After oxidation of Ca depleted steel slag at 250°C in acetic acid (1 M)
Calcite – $CaCO_3$	+++	+++	–	–
Portlandite – $Ca(OH)_2$	++	+	–	–
Larnite – Ca_2SiO_4	+++	–	–	–
Brownmillerite – $Ca_2Fe_{1.8}Al_{0.2}O_5$*	+++	–	+++	–
Wüstite – $Fe_{0.52}Mg_{0.48}O$*	++	+	+++	–
Magnetite – Fe_3O_4	+	++	+	+++
Aragonite – $CaCO_3$	+	-	–	–
Vaterite – $CaCO_3$	+	-	–	–
Quartz – SiO_2	(+)	-	–	–
Hydroxylapatite – $Ca_5(PO_4)_3(OH)$	+	++	–	++
Hibschite – Katoite $Ca_3Al_2(SiO_4)_{3-x}(OH)_{4x}$	–	+++	–	–
Jaffeite – $Ca_6Si_2O_7(OH)_6$	–	++	–	–
Brucite – $Mg(OH)_2$	–	+	–	–
Chlorite phase – $(Fe,Mg,Al)_6(Si,Al)_4O_{10}(OH)_8$	–	–	–	+++
Hematite – Fe_2O_3	–	–	–	++

FIGURE 1 | (A) Hydrogen production monitored as a function of time at 250°C (diamonds, APW-250C), 300°C (circles, APW-300C) and 350°C (squares, APW-350C) from steel slag hydrothermal oxidation in de-ionized water; pressure reached 160 to 190 bar after heating; (B) Arrhenius plot of the retrieved kinetic constants using a square-root rate law.

Assuming an Arrhenius behavior, an activation energy of 28 ± 4 kJ/mol is retrieved (**Figure 1B**).

$$H_2(t) = A_n t^{0.5} \qquad (2)$$

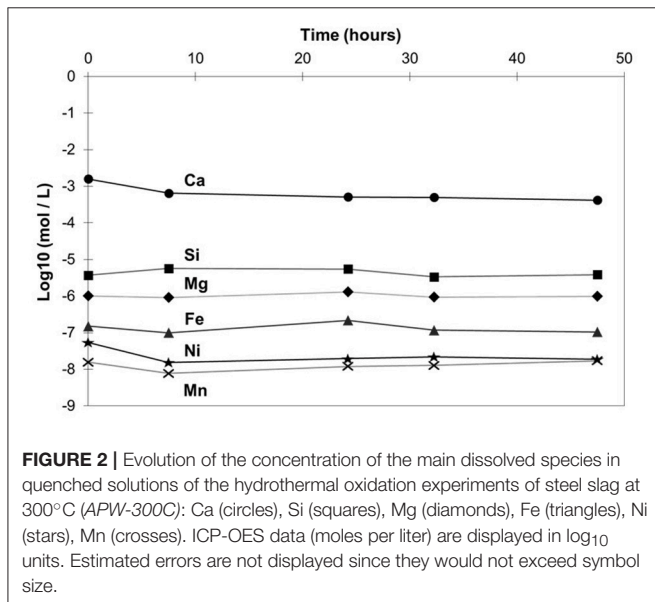## Steel Slag Hydrothermal Oxidation at 300°C: Aqueous Speciation and Mineralogical Changes

The steel slag oxidized at 300°C was further characterized (APW-300C). Time-resolved composition of the aqueous solution was monitored by ICP-OES (**Figure 2**). By order of abundance, Ca, Si, Mg, Fe, Ni, and Mn were found to be the main dissolved components. Their concentrations remained roughly stable as reaction proceeded. Average calcium concentration reached 10^{-3} mol/L whereas iron concentration was close to 10^{-7}M and so could not be quantified by the complexation–UV spectroscopy method. An estimated pH of 11 is obtained from the measured Ca concentration (assumed to occur as $Ca^{2+}_{,aq}$) and neglecting possible CO_2 aqueous species.

XRPD was conducted on dried solid sample (**Figure 3**). Mineral modes obtained from semi-quantitative Rietveld

TABLE 3 | Experimental conditions and measured H$_2$ yield in experiments performed in the sampling autoclave.

Sample name	Medium	Temperature (°C)	Pressure (bar)	Total reaction time (h)	H$_2$ yield at the end of experiment (g H$_2$/kg FeO)	FE-SEM investigations
APW-250C	Water	250	190	70.5	0.87	
APW-300C	Water	300	190	70.5	2.13	x
APW-350C	Water	350	230	79.5	8.07	
APAc-1M-250C	1 M acetic acid	250	180	51	6.93	x

FIGURE 2 | Evolution of the concentration of the main dissolved species in quenched solutions of the hydrothermal oxidation experiments of steel slag at 300°C (*APW-300C*): Ca (circles), Si (squares), Mg (diamonds), Fe (triangles), Ni (stars), Mn (crosses). ICP-OES data (moles per liter) are displayed in log$_{10}$ units. Estimated errors are not displayed since they would not exceed symbol size.

refinement are presented in **Table 2**. Although Ca-species dominate in the HP-HT solution (**Figure 2**), CaO remains the main oxide component in the solid residue after hydrothermal oxidation. Members of the hibschite-katoite series Ca$_3$Al$_2$(SiO$_4$)$_{3-x}$(OH)$_{4x}$ were found to represent the dominant mineral phases. Jaffeite, an hydrated calcium silicate Ca$_6$Si$_2$O$_7$(OH)$_6$, was also detected. Calcium is also found in calcite, portlandite and hydroxylapatite. Iron was only detected as wüstite and magnetite. Minor brucite, Mg(OH)$_2$, is observed.

Magnetite: Separation and Observations

In addition to hydrogen production, steel slag hydrothermal oxidation led to the formation of magnetite as shown by XRPD (**Figure 3**). In order to better characterize the magnetite component of the experimental product, the magnetite fraction was separated using a two-step magnetic separation procedure, respectively in water and in a 2% hydrochloric solution. The result of the first step of separation in water can be evaluated on **Figure 4** where magnetite represents now, by far, the dominant mineral constituent. However, many other calcium-bearing phases initially present in oxidized steel slag remained. Consequently, a second magnetic separation step was performed in dilute hydrochloric acid in order to dissolve and remove these unwanted phases. A solid fraction composed of only magnetic oxides was successfully recovered (**Figure 5a**). From Rietveld

semi-quantitative analysis, magnetite was found to represent 80 wt.% of the sample whereas the remaining 20 wt.% are assigned to wüstite.

Images of the separated iron oxide particles are displayed on **Figures 5b,c**. Particles were found to fall in three size ranges: 10–30 nm, 100–300 nm, and 1–10 μm. Cubic shaped particles are dominant within the 10–30 nm range. Flat and needle shaped particles are predominant in the 100–300 nm range. SAED pattern was obtained from a single nanoparticle and indexed as magnetite (**Figure 5d**). However, note that the SAED pattern is also close to that of maghemite.

Steel Slag Oxidation in Acetic Acid Media

A total of six runs was performed in gold capsule on the starting steel slag in acetic acid solutions at 150 and 300°C for 72 h with concentrations of 1, 2, and 4 M. H$_2$ was produced in every experiments (**Table 4**). At 150°C, only 0.15 and 0.17 g H$_2$/kg FeO equivalent were respectively produced at initial concentrations of 1 and 2 M, i.e., far less than the calculated maximum of 9.28 g H$_2$/kg FeO equivalent. At 4 M and for the same temperature, 1.14 g H$_2$/kg FeO were produced, i.e., 10 times higher than for the lower acetic acid concentrations. At 300°C, hydrogen production rates increased significantly. Respectively, 3.43, 4.33, and 3.08 g H$_2$/kg FeO equivalent were produced for acetic acid initial concentrations of 1, 2, and 4 M. At 4 M, methane was detected in addition to H$_2$.

After H$_2$ gas analysis, solid samples were dried and analyzed using XRPD. Patterns of starting and oxidized steel slag in presence of acetic acid at 1, 2, and 4 M are compared in **Figure 6**. Due to the limited amount of material recovered from the capsules, no Rietveld analysis has been undertaken. Relative variations of wüstite and magnetite can be examined qualitatively on the basis of selected reflection on the XRPD pattern. The 220 and 311 reflexions of magnetite as well as the 200 and 111 reflexions of wüstite were chosen (**Figure 6**). After oxidation at 150°C, only small changes were observed at 1 and 2 M with a decrease of wüstite Bragg's peaks and a slight increase of magnetite ones. This trend is clearly visible at 4 M however with the intensity of the 111 wüstite reflection which has significantly decreased. At 300°C, the evolution observed at 150°C becomes obvious. The higher the concentration, the less the residual wüstite and the more defined and intense the magnetite peaks. At 300°C for a 4 M acid acetic solution, no more wüstite is detected with XRPD (**Figure 6**). The oxidation of wüstite is apparently more pronounced at 1 M and 300°C than at 4 M and 150°C. Runs performed at 300°C were also marked by
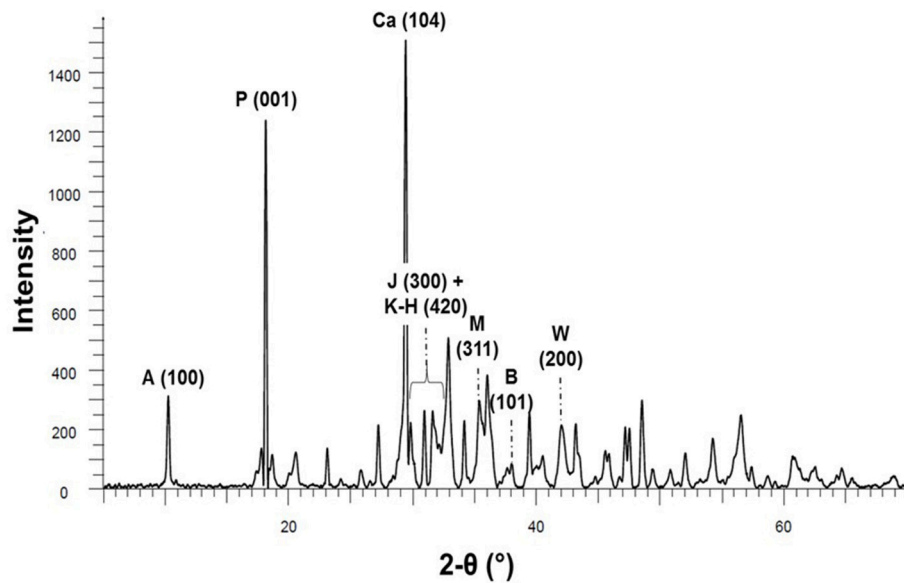
FIGURE 3 | XRPD pattern of hydrothermally oxidized steel slag (300°C−190 bar, *APW-300C*), the most intense peak of every identified crystalline phases is labeled (see **Table 2**) as follows: hydroxylapatite (A), portlandite (P), calcite (Ca), jaffeite (J), katoite-hibschite series (K-H), magnetite (M), brucite (B), and wüstite (W).
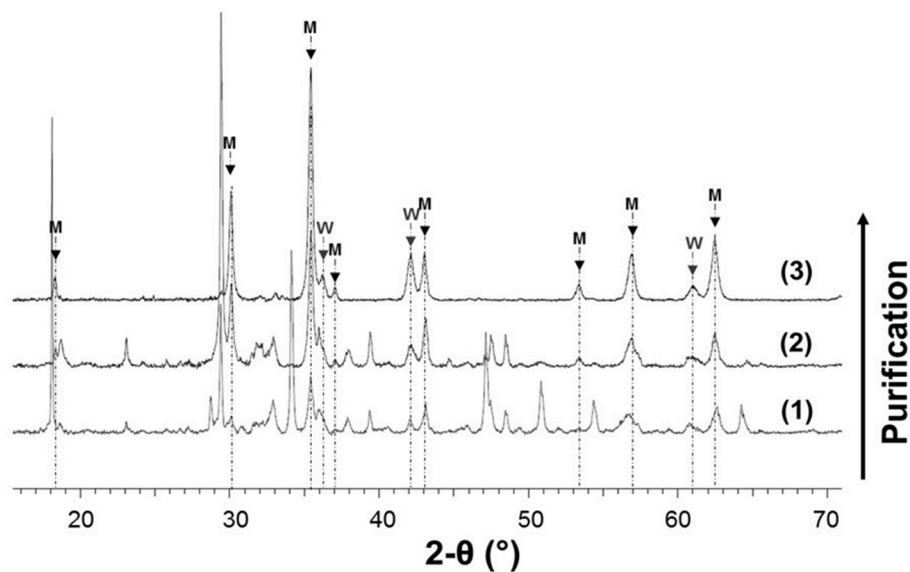

FIGURE 4 | XRPD patterns before and after the two magnetic separation steps; (1) oxidized steel slag before separation (*APW-300C*); (2) solid fraction after the first magnetic separation in water; (3) solid fraction after the second separation step in HCl (2%); M and W stand for magnetite and wüstite, respectively; unidentified peaks in (1) and (2) are related to calcium-bearing phases initially present in the hydrothermally treated steel slag (see **Table 2**).

the crystallization of a significant amount of brucite, $Mg(OH)_2$ (**Figure 6**).

Oxidation Kinetics of Decalcified Steel Slag
Ca Removal with Acetic Acid

Steel slag was reacted with 500 ml solution of 4 M acetic acid at ambient temperature for 60 min in order to dissolve portlandite, calcite and larnite. Chemical analyses performed by μXRF before and after the treatment (**Table 1**) confirmed the selective dissolution of Ca and Si; Ca and Si contents were divided by 2.5 and 1.5, respectively. Every other oxide proportions were subsequently increased by a factor of about 2. Mineralogical changes were inspected using XRPD (**Table 2**). After acetic acid attack, only iron-bearing oxides were found as residual crystalline phases; wüstite and brownmillerite are the dominant mineral phases which coexist
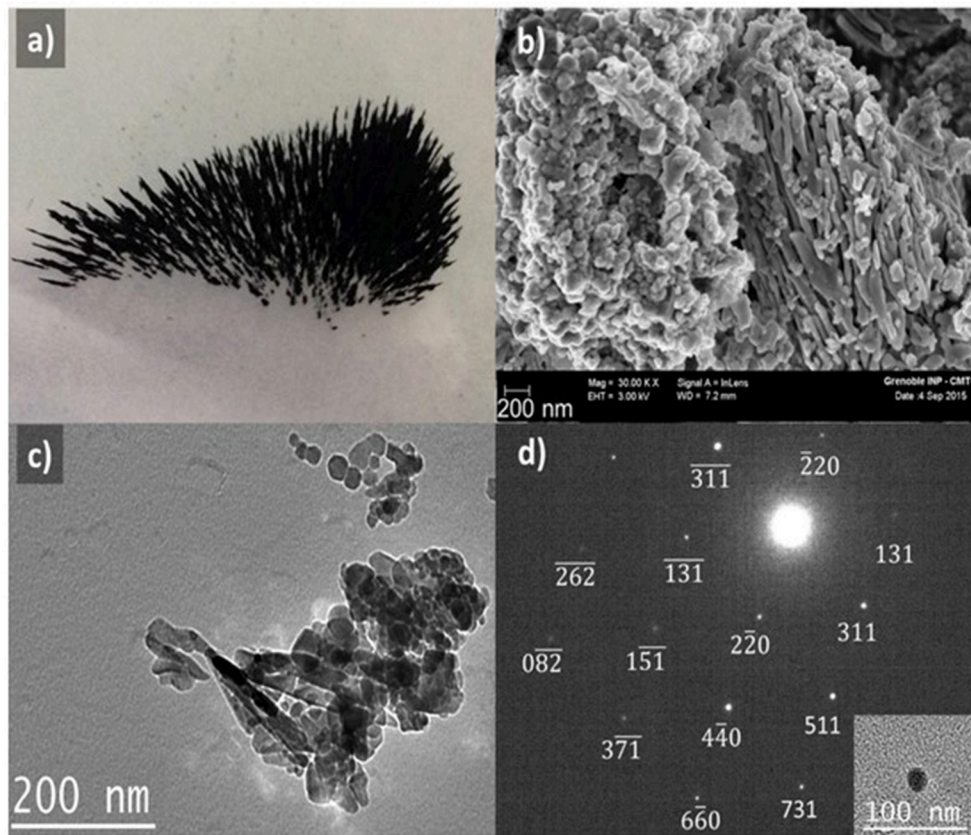
FIGURE 5 | Observation of magnetic particles after separation from *APW-300C* sample; **(a)** optical image (with a total length of about 5 cm); **(b)** FE-SEM and **(c)** TEM images; **(d)** Electron micro-diffraction pattern of an isolated magnetite nanoparticle visible in the lower-right panel with the corresponding scale bar.

with minor magnetite whereas no more crystalline silicates were detected.

Time-Resolved Monitoring of H$_2$ Production and Fe^{2+} Aqueous Concentration

Hydrothermal oxidation of the decalcified steel-slag sample was performed at 150 and 250°C in a sampling autoclave with a 1 M acid acetic solution (*APAc-1M-250C* sample). Under such acidic conditions, the hastelloy^{TM} autoclave may itself react with the solution and produce H$_2$. A blank run with the same amount of 1 M solution was performed at 150 and 250°C. Whereas no H$_2$ was produced by the metal of the autoclave at 150°C, a total of about 1 mmol H$_2$ was produced after 51 h at 250°C (**Figure 7**). It should however be noted that this H$_2$ yield produced by the autoclave oxidation with pure 1 M acetic solution is an upper bound to the effective autoclave contribution in the presence of a slag sample since the partial dissolution of the latter will increase the pH of the reacting solution.

Around 2 g of decalcified slag was first oxidized for 24 h at 150°C. No H$_2$ was detected at this temperature (**Figure 7**). Ferrous iron dissolution occurred to a level of 8.10^{-4} M (**Figure 7**) corresponding to less than 2 mol.% of the bulk iron content of the slag.

In the absence of significant reaction, temperature was then raised to 250°C. Pressure was decreased before heating in order to reach 180 bar at 250°C. Immediately after reaching 250°C, hydrogen production started at a roughly constant rate until a plateau of H$_2$ concentration was attained after an overall run duration of 72 h (i.e., after 48 h at 250°C). A yield of 6.93 g H$_2$/kg FeO equivalent is achieved after 75 h (i.e., 51 h at 250°C, **Table 3**) which, again, includes the H$_2$ arising from the autoclave corrosion under acidic conditions.

In parallel, ferrous concentration increased by one order of magnitude to reach 8.10^{-3} M at 250°C. Ferrous iron concentration remained roughly constant until the end of experiment. A constant pH of 4 was measured at ambient in aqueous aliquots sampled at 150 and 250°C.

Characterization of the Solid Products

XRPD analysis was performed on the decalcified sample after its oxidation at 250°C in a 1 M acetic acid solution (**Figure 8**). Only three iron-bearing phases were identified: hematite, magnetite and a chlorite-group mineral with its characteristic 14 Å basal reflection. Phase abundances are presented in **Table 2** but have to be considered with caution due to the unknown composition of the observed chlorite.

TABLE 4 | Measured hydrogen production after hydrothermal oxidation of steel slag in the presence of acetic acid; experiments were performed in gold capsules.

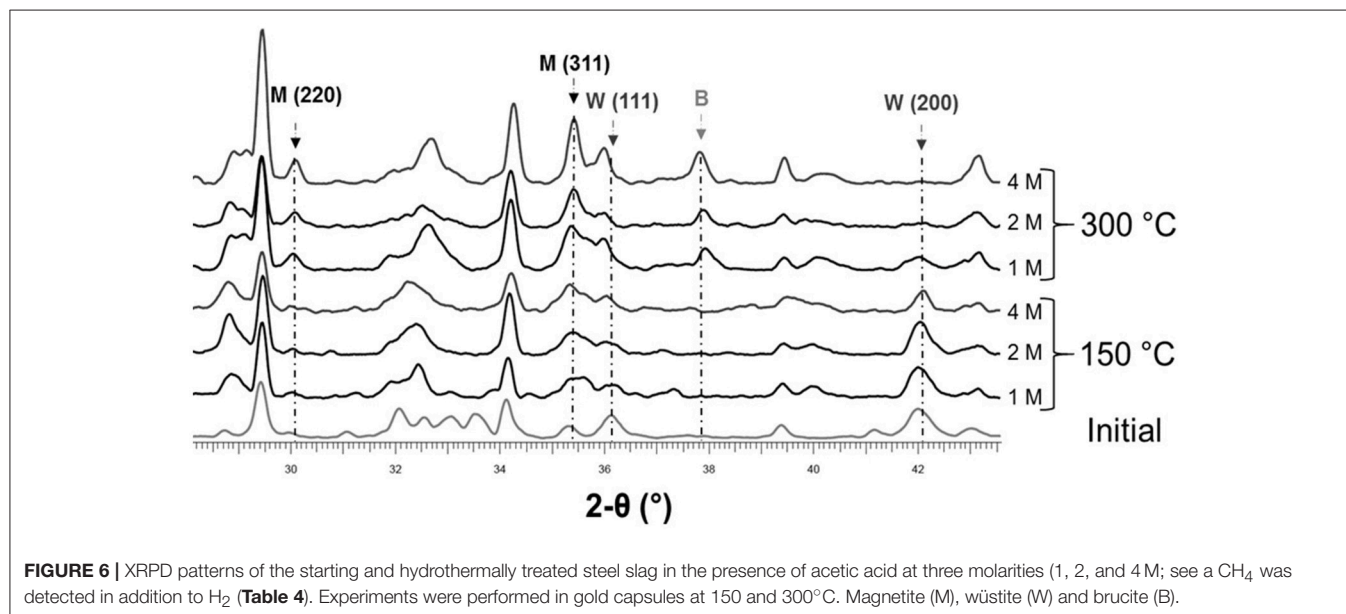| Sample name	Temperature (°C)	Reaction time (h)	Pressure (bar)	Acetic acid concentration (mol/L)	H_2 yield (g H_2/kg FeO)
CAc-1M-150C	150	72	300	1	0.15
CAc-2M-150C	150	72	300	2	0.17
CAc-4M-150C	150	72	300	4	1.14
CAc-1M-300C	300	72	300	1	3.43
CAc-2M-300C	300	72	300	2	4.33
CAc-4M-300C	300	72	300	4	3.08[a]

[a]CH_4 was detected in addition to H_2.

FIGURE 6 | XRPD patterns of the starting and hydrothermally treated steel slag in the presence of acetic acid at three molarities (1, 2, and 4 M; see a CH_4 was detected in addition to H_2 (**Table 4**). Experiments were performed in gold capsules at 150 and 300°C. Magnetite (M), wüstite (W) and brucite (B).

FE-SEM investigations were performed on the recovered particles without preliminary magnetic separation (**Figure 9**). Clusters of 5–50 nm magnetite particles with octahedral morphologies were easily found. Larger particles ranging from 100 to 300 nm with sheet-like morphologies were also observed which are interpreted as chlorite.

Chemical analysis performed by μXRF on the retrieved solid sample showed results closed to the decalcified steel slag before oxidation. Differences were mainly found in the unexpected presence of Ni (autoclave contamination) and the decrease in Mg and Ca.
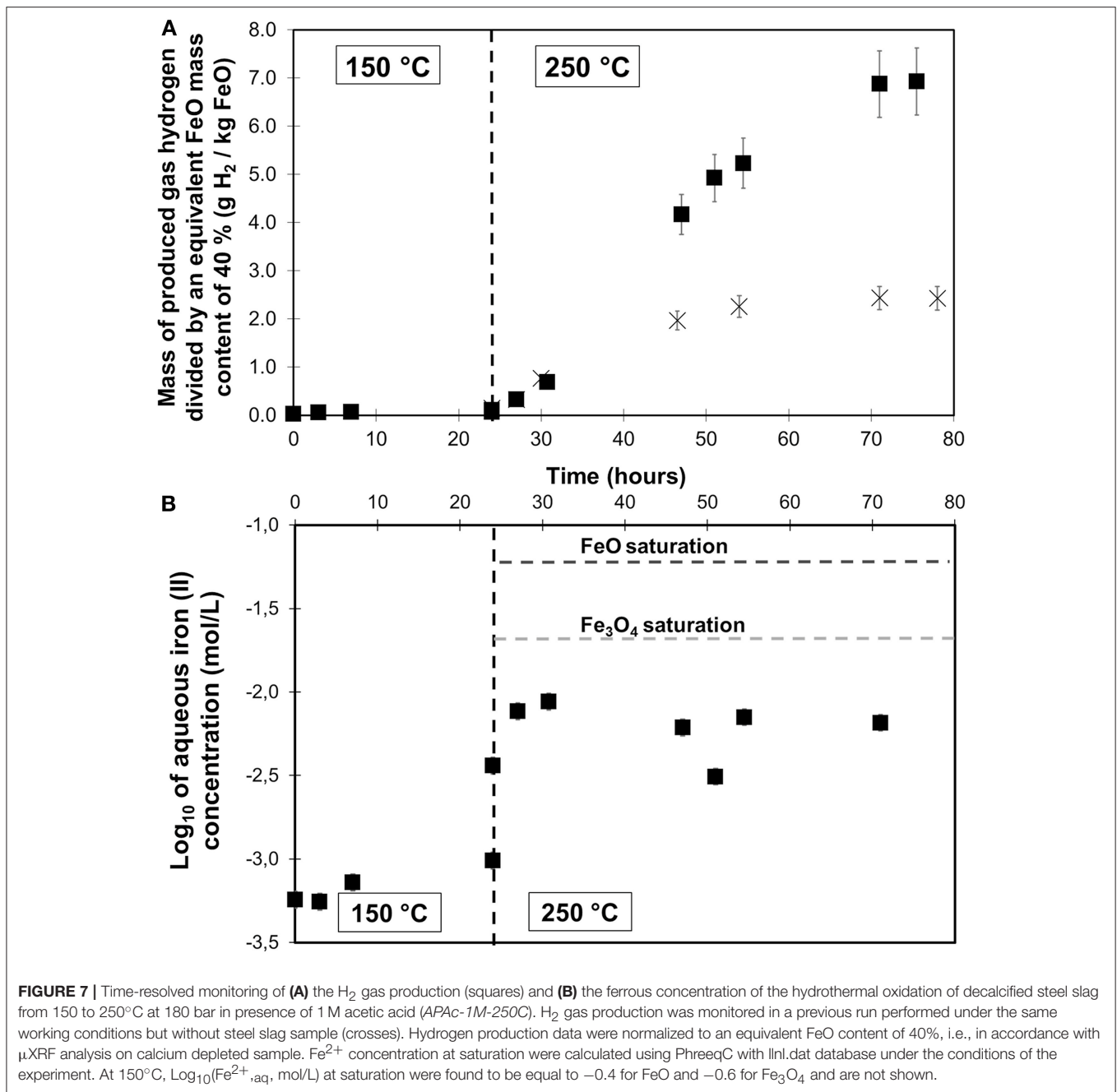
DISCUSSION

Hydrothermal Slag Oxidation Kinetics: Effect of Temperature and pH

Hydrothermal Oxidation of Steel Slag in Water: Comparison with Reagent Grade Feo and Influence of Temperature

Hydrogen production kinetics associated with the hydrothermal oxidation of a relatively fresh BOF steel slag sample (a few weeks of storage in open air) in de-ionized water has been studied at 250, 300, and 350°C (**Figure 1**). A similar overall kinetic behavior was observed at the three temperatures with the highest H_2 production rate encountered during the first 24 h, which progressively decreased for longer run duration. A very similar kinetic behavior was described by Crouzet et al. (2017) for reagent grade FeO reacting with pure water at 300°C. Even the H_2 yield normalized to bulk FeO content is very close at 300°C; after about 72 h, 2.13 g H_2/kg FeO equivalent were produced from steel slag oxidation whereas about 1.9 g H_2/kg FeO were found from FeO reagent grade oxidation. Two different models however were used to fit the FeO and steel slag oxidation kinetics. Steel-slag oxidation kinetics could not be successfully fitted to a first-order kinetic model, at least for the investigated run duration. Instead, H_2 production kinetics for steel slag were fitted to a simple square root function of time. After 72 h of reaction, 0.87, 2.13, and 8.07 g H_2/kg equivalent FeO were respectively produced at 250, 300, and 350°C (**Figure 1A**). Increasing the temperature led to higher H_2 production. By fitting steel slag oxidation kinetics with a square root model and assuming an Arrhenius behavior, an activation energy of 28 ± 4 kJ/mol was retrieved (**Figure 1B**). This value is in line with range of activation energies reported by Malvoisin et al. (2013), of 15 ± 2 and 41 ± 12 kJ/mol for uncarbonated and carbonated BOF slag, respectively.

FIGURE 7 | Time-resolved monitoring of **(A)** the H_2 gas production (squares) and **(B)** the ferrous concentration of the hydrothermal oxidation of decalcified steel slag from 150 to 250°C at 180 bar in presence of 1 M acetic acid (*APAc-1M-250C*). H_2 gas production was monitored in a previous run performed under the same working conditions but without steel slag sample (crosses). Hydrogen production data were normalized to an equivalent FeO content of 40%, i.e., in accordance with μXRF analysis on calcium depleted sample. Fe^{2+} concentration at saturation were calculated using PhreeqC with llnl.dat database under the conditions of the experiment. At 150°C, $Log_{10}(Fe^{2+},_{aq}, mol/L)$ at saturation were found to be equal to −0.4 for FeO and −0.6 for Fe_3O_4 and are not shown.

On the only basis of two temperatures, the temperature dependence of steel slag oxidation kinetics as measured in the sampling autoclave is confirmed in experiments with acetic acid performed in gold capsule. Retrieved H_2 production yields were respectively multiplied by 23 and 25 at 1 and 2 M by raising the temperature from 150 to 300°C, corresponding to an approximate activation energy in the order of 20 kJ/mol. Moreover, Crouzet et al. (2017) found an activation energy of 27 kJ/mol for the oxidation of FeO in the presence of 0.05 M acetic acid in gold capsule. This activation energy does not allow to extrapolate oxidation kinetics obtained below 300°C toward higher temperature due to the likely thermal decomposition

of acetic acid. However, it can be tentatively concluded that the clustering of activation energies around 30 kJ/mol for the production reaction of H_2 in steel slag and pure FeO, with or without acid acetic addition, is an indication of the same rate-limiting process, i.e., the ferrous iron dissolution from the wüstite component.

Oxidation Kinetic Improvement in Presence of Acetic Acid: pH and Aqueous Speciation

Crouzet et al. (2017) reported that iron dissolution is the rate limiting factor for the hydrothermal H_2 production from FeO in similar P-T conditions as those investigated here.
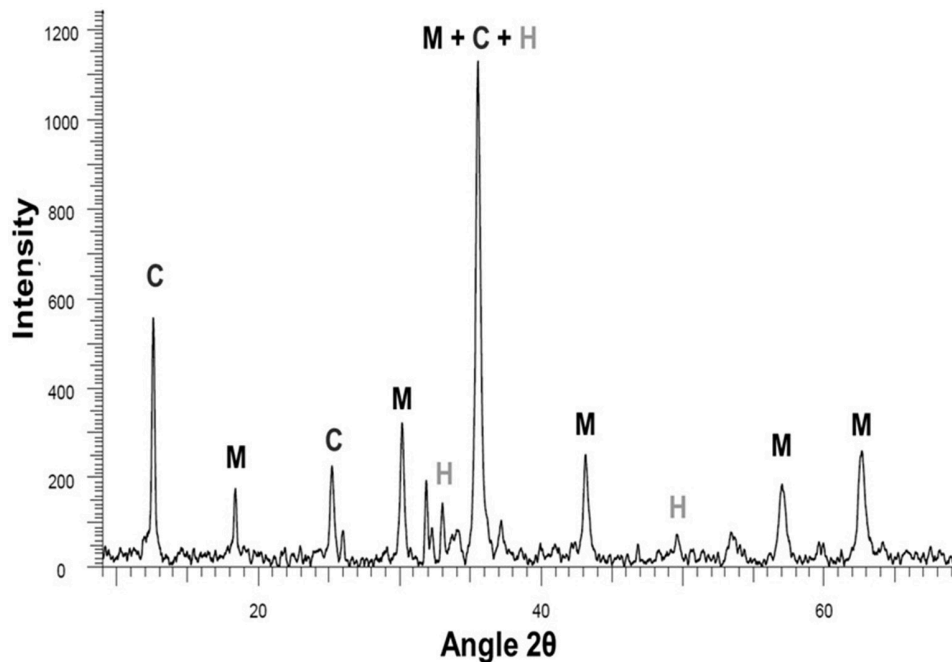
FIGURE 8 | XPRD pattern of decalcified steel slag after hydrothermal oxidation at 250°C in 1 M acetic acid solution: magnetite (M), chlorite (C), and hematite (H).
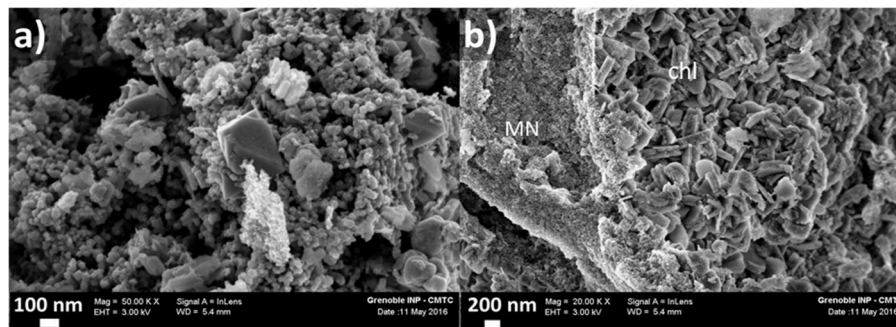

FIGURE 9 | FE-SEM imaging of solid samples recovered after hydrothermal oxidation at 250°C in 1 M acetic acid solution; **(a)** magnetite nanoparticle clusters; **(b)** magnetite nanoparticles (MN) and lamellar nanoparticles interpreted as chlorite (chl).

They showed that the presence of mild acetic acid solution significantly enhances iron dissolution kinetics owing to a ligand-promoted dissolution process (Stumm, 1997; Hamer et al., 2003).

However, using the same acid acetic concentration will definitely not yield the same pH conditions in the case of the steel slag due to its high alkalinity (Huijgen and Comans, 2005; Malvoisin et al., 2013; Costa et al., 2016; Crouzet et al., in press). In order to achieve acidic conditions during steel slag oxidation with an in-situ pH < 5–6, two routes were tested through (1) the use of concentrated acetic acid to ensure the dissolution of all the Ca of the steel slag and (2) calcium removal at room temperature followed by the oxidation of the solid residue in a 1 M acetic acid solution.

For both routes, a clear kinetics enhancement has been noticed at 250 and 300°C. At 150°C, however, on the contrary to what

has been found for reagent grade FeO (Crouzet et al., 2017), no significant H$_2$ production has been detected.

H$_2$ production and Fe(II) dissolution in 1 M acetic acid solution from Ca depleted steel slag sample have both been monitored in the sampling autoclave at a temperature initially fixed to 150°C and then raised to 250°C due to the absence of H$_2$ production (**Figure 7**). Aqueous iron saturation with respect to FeO and Fe$_3$O$_4$ in 1 M acetic acid has been calculated at 150 and 250°C and compared to the experimental data. Furthermore, at both temperatures, assuming that the slag is only composed of FeO and Fe$_3$O$_4$ and neglecting the effect of residual Ca, an in-situ pH in the 3.9–5.2 range is calculated which consistent with the pH of ca. 4 determined on aqueous aliquot after cooling. At 150°C, no significant H$_2$ is produced and the Fe^{2+} aqueous concentration remains at the 8.10^{-4}M level. Aqueous Fe concentration at 150°C is by one to two orders of

magnitude below Fe_3O_4 and FeO saturation, respectively. Either aqueous Fe is controlled by the solubility of a less soluble iron oxide/hydroxide phase(s) or the aqueous Fe content is limited by the slow FeO dissolution at this temperature. The fact that magnetite supersaturation is not attained is consistent with the absence of H_2 production. The situation becomes different once T is increased to 250°C. H_2 production starts to proceed and Fe^{2+} aqueous concentration increases by one order of magnitude to reach 8.10^{-3}M which corresponds to magnetite saturation. FeO dissolution and Fe_3O_4 precipitation processes are thus triggered. Contrary to what has been observed by Crouzet et al. (2017) with respect to the hydrothermal oxidation rate of pure FeO at 150°C, FeO dissolution is not fast enough to produce significant magnetite supersaturation. These results on decalcified steel slag confirmed, however, the positive effect of acidic pH and acetic acid on the hydrothermal oxidation kinetics of FeO.

The positive effect of acetic acid on H_2 production was also evidenced from the oxidation experiments performed in gold capsules on native steel slag samples in the presence of concentrated acetic acid solutions. At 300°C, H_2 yield at 1, 2, and 4 M in gold capsules was found to be about four times higher than in the experiment performed with distilled water in the sampling autoclave. The effect of concentrated acid acetic might even be larger considering the fact that capsule experiments have a lower H_2 yield compared to sampling autoclave experiments (Crouzet et al., 2017). Finally, H_2 yields were also found to increase with initial acetic acid concentrations at 150 and 300°C.

Magnetite Valorization
Formation of Magnetite Nanoparticles
By combining GC analysis of H_2 and saturation magnetization (Js, see Malvoisin et al., 2012 for the method), Malvoisin et al. (2013) showed a one to one molar relationship between H_2 and magnetite production in a BOF slag treated hydrothermally (pure water) in gold capsule using externally heated pressure vessels. However, Malvoisin et al. (2013) focused on H_2 as valuable product but did not consider the potential value of magnetite and they therefore overlooked grains with the smallest sizes. The identification, here, of abundant magnetite with sizes below 1 µm opens the way to a new valorization of steel slags owing to the multiple applications of magnetite in the industry (see Introduction section).
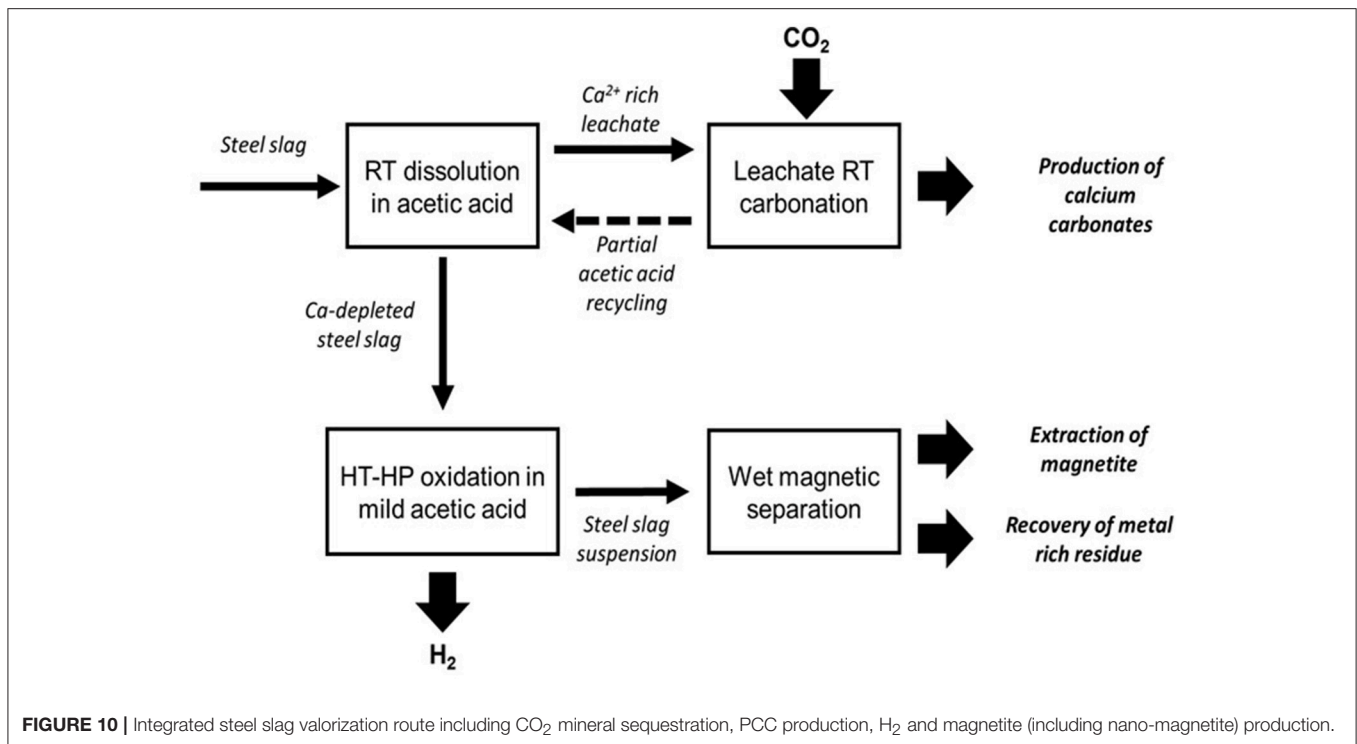
By applying a simple wet magnetic separation with a permanent magnet, we succeeded in extracting from the hydrothermally oxidized slag (pure water) an iron oxide-rich product containing a high magnetite proportion (**Figure 4**). FE-SEM and TEM imaging revealed that most of the newly formed magnetite crystals occur as nanoparticle agglomerates (**Figure 5**) in both original steel slag and decalcified samples, i.e., at basic and acidic pH values. Three main granulometric classes were identified: 10–30 nm, 100–300 nm, and 1–10 µm. Most of the particles display an octahedral morphology as it is usually encountered for grains of that size (Sun and Zeng, 2002; Daou et al., 2006; Horak et al., 2007; Iida et al., 2007). Needle-shaped grains are also observed whereas such morphology was neither observed in iron oxides produced hydrothermally from FeO (Crouzet et al., 2017) nor in steel slags oxidized with a CO_2 partial pressure (Crouzet et al., in press).

Due to its applications in medicine as contrast agent, a considerable number of studies were dedicated to the synthesis of magnetite nanoparticles (Daou et al., 2006; Gnanaprakash et al., 2007; Iida et al., 2007; Ge et al., 2009). Most of the syntheses are based on the co-precipitation method. This method consists in the dissolution of a stoichiometric mixture of ferrous and ferric salts in aqueous solution. The pH is then increased through the addition of a base (NH_4OH, $N(CH_3)_4OH$, $H_2N(CH_2)_6NH_2$...) to instantaneously decrease the iron solubility and promote the precipitation of magnetite nanoparticles. The particle size distribution was found to be dependent upon the initial proportion of ferrous ions in the starting solution (Iida et al., 2007). Higher ferrous initial proportion leads to the formation of smaller particles. To get larger particles and reduce their dispersity, Daou et al. (2006) proposed to perform an additional hydrothermal step at a temperature of 250°C. Particles centered on 39 nm were then obtained. Ge et al. (2009) proposed to use only ferrous salt as starting material. After the addition of the base under vigorous stirring in air and the formation of a magnetite suspension, hydrothermal conditions (134°C) are applied. The authors also confirmed the effect of the initial ferrous salt concentration on the size distribution.

As the co-precipitation method, the production of magnetite from hydrothermal steel slag oxidation occurred through a dissolution—precipitation process for which dissolution was identified as the limiting factor in pure water. Iron speciation and concentration (supersaturation level) are however drastically different when nanomagnetite particles are synthesized from hydrothermal oxidation of steelmaking slags and from co-precipitation methods. Due to the relatively high pH imposed by native steel slag, aqueous iron concentration remains very low, even at high temperature, e.g., 10^{-7} M of ferrous iron was encountered at 300°C. Contrary to the co-precipitation method, magnetite particles were not all produced simultaneously but over the whole oxidation reaction as shown with the time-resolved monitoring of hydrogen production. This particularity likely contributes to the formation of the observed particle size distribution. The largest micrometric particles may be related to the magnetite particles initially present in steel slag and which possibly grew during the whole hydrothermal treatment possibly by Ostwald ripening.

Toward an Integrated Steel Slag Valorization Chain
Valorization of steel slag through hydrothermal oxidation leads to the simultaneous production of hydrogen and magnetite. According to the World Steel Association (2015), more than 1.4 billion tons of steel were annually produced since 2010 in the world. Steel slag production represents 10–15% by weight of steel output (van Oss, 2013), being 140 to 220 Mt each year. Considering a mean FeO content of 22.9 wt.% in steel slags (Piatak et al., 2015), from 300 to 470 kt H_2 and 35 to 54 Mt Fe_3O_4 may be produced at most through the hydrothermal treatment of the current annual steel slag production. In comparison, the Australian Ridley Magnetite mining project proposed the exploitation of 48 Mt magnetite ore per annum over 30 years for a capital requirement estimated in 2009 to about 3 billion Australian dollars (Atlas Iron Company, 2009).

FIGURE 10 | Integrated steel slag valorization route including CO_2 mineral sequestration, PCC production, H_2 and magnetite (including nano-magnetite) production.

In order to develop a competitive valorization path, we proposed a process that includes (1) the recovery and separation of magnetite particles and (2) the use of acidic conditions in the hydrothermal oxidation step (**Figure 10**). Moreover, calcium removal with acetic acid, prior to the hydrothermal step, turned out to significantly increase the oxidation reaction kinetics. Furthermore, valuable high-purity PCC can be obtained by RT carbonation of the Ca-acetate solution and acetic acid can then be regenerated (Teir et al., 2007, 2011; Eloneva et al., 2008). The decalcified steel slag can be processed hydrothermally with a low-concentration acetic acid solution, at a pH below 5, in order to improve the ferrous iron oxidation kinetic by increasing the iron dissolution rate (Crouzet et al., 2017). Finally, we propose to extract the magnetite fraction from the processed steel slag by magnetic separation.

Obviously, the parameters of the process still need to be improved in order to optimize either the amount of sequestered CO_2, H_2 yield and purity, or the magnetite size distribution. In particular, the final magnetic separation step must be improved and adapted to the separation of nanoparticles. The High Gradient Magnetic Separation (HGMS) technique seems the most suitable to date and has already shown spectacular results in medical applications with the separation of magnetite nanoparticle fractions from each other (Oberteuffer, 1973; Kelland et al., 1975; Kelland, 1998).

CONCLUSION

We reported here an enhanced process for steel slag valorization through the hydrothermal oxidation of its ferrous iron content.

Two routes were investigated to complement and improve the method proposed by Malvoisin et al. (2013). We focused on the characterization/separation of the produced magnetite for its significant economic value. In particular, the nanometer fraction of the recovered magnetite is suitable for high-technology applications (medicine, electronic, mechanical engineering...). We also show the use of acetic acid at the vinegar concentration level on decalcified slag to increase the H_2/magnetite production kinetics by around one order of magnitude. The preliminary slag decalcification is a requisite which however offers a way to sequester the CO_2 in a solid product (PCC) that can be used in the industry (Teir et al., 2007, 2011; Eloneva et al., 2008).

AUTHOR CONTRIBUTIONS

CC carried experiments and characterization, FB supervised this work, AA ran the TEM, NF carried out XRPD and Rietveld analysis, VM performed XRF, NR was involved in the RedOx chemistry, JF helped at defining valorization processes, BG dealt with nanomagnetite applications.

ACKNOWLEDGMENTS

REFERENCES

Ahles, C. C. (1946). *Ballast Block*. Patent No. US2409094 A.

Charlou, J. L., Donval, J. P., Fouquet, Y., Jean-Baptiste, P., and Holm, N. (2002). Geochemistry of high H2 and CH4 vent fluids issuing from ultramafic rocks at the rainbow hydrothermal field (36°14'N, MAR). *Chem. Geol.* 191, 345–359. doi: 10.1016/S0009-2541(02)00134-1

Costa, G., Polettini, A., Pomi, R., and Stramazzo, A. (2016). Leaching modelling of slurry-phase carbonated steel slag. *J. Hazard. Mater.* 302, 415–425. doi: 10.1016/j.jhazmat.2015.10.005

Creutz, E., and Downes, K. (1949). Magnetite concrete for radiation shielding. *J. Appl. Phys.* 20, 1236–1240. doi: 10.1063/1.1698315

Crouzet, C., Brunet, F., Montes-Hernandez, G., Recham, N., Findling, N., Ferrasse, J.-H. et al. (in press). Hydrothermal steel slag valorization: Part I. Coupled H₂ production and CO₂ mineral sequestration. *Front. Energy Res.*

Crouzet, C., Brunet, F., Recham, N., Findling, N., Lanson, M., Guyot, F., et al. (2017). Hydrogen production by hydrothermal oxidation of FeO under acidic conditions. *Int. J. Hydrog. Energy* 42, 795–806. doi: 10.1016/j.ijhydene.2016.10.019

Daou, T. J., Pourroy, G., Bégin-Colin, S., Grenèche, J. M., Ulhaq-Bouillet, C., Legaré, P., et al. (2006). Hydrothermal synthesis of monodisperse magnetite nanoparticles. *Chem. Mater.* 18, 4399–4404. doi: 10.1021/cm060805r

Drozdov, A. S., Ivanovski, V., Avnir, D., and Vinogradov, V. (2016). A universal magnetic ferrofluid: nanomagnetite stable hydrosol with no added dispersants and at neutral pH. *J. Colloid Interf. Sci.* 468, 307–312. doi: 10.1016/j.jcis.2016.01.061

Eloneva, S., Teir, S., Salminen, J., Fogelholm, C.-J., and Zevenhoven, R. (2008). Steel converter slag as a raw material for precipitation of pure calcium carbonate. *Ind. Eng. Chem. Res.* 47, 7104–7111. doi: 10.1021/ie8004034

Gawande, M. B., Branco, P. S., and Varma, R. S. (2013). Nano-magnetite (Fe₃O₄) as a support for recyclable catalysts in the development of sustainable methodologies. *Chem. Soc. Rev.* 42:3371. doi: 10.1039/c3cs35480f

Ge, S., Shi, X., Sun, K., Li, C., Uher, C., Baker, J. R., et al. (2009). Facile hydrothermal synthesis of iron oxide nanoparticles with tunable magnetic properties. *J. Phys. Chem. C* 113, 13593–13599. doi: 10.1021/jp902953t

Gnanaprakash, G., Mahadevan, S., Jayakumar, T., Kalyanasundaram, P., Philip, J., and Raj, B. (2007). Effect of initial pH and temperature of iron salt solutions on formation of magnetite nanoparticles. *Mater. Chem. Phys.* 103, 168–175. doi: 10.1016/j.matchemphys.2007.02.011

Hacker, V., Fankhauser, R., Faleschini, G., Fuchs, H., Friedrich, K., Muhr, M., et al. (2000). Hydrogen production by steam–iron process. *J. Power Sources* 86, 531–535. doi: 10.1016/S0378-7753(99)00458-9

Hamer, M., Graham, R. C., Amrhein, C., and Bozhilov, K. N. (2003). Dissolution of Ripidolite (Mg, Fe-Chlorite) in organic and inorganic acid solutions. *Soil Sci. Soc. Am. J.* 67:654. doi: 10.2136/sssaj2003.6540

Horak, D., Babic, M., Mackova, H., and Benes, M. J. (2007). Preparation and properties of magnetic nano- and microsized particles for biological and environmental separations. *J. Sep. Sci.* 30, 1751–1772. doi: 10.1002/jssc.200700088

Hua, M., Zhang, S., Pan, B., Zhang, W., Lv, L., and Zhang, Q. (2012). Heavy metal removal from water/wastewater by nanosized metal oxides: a review. *J. Hazard. Mater.* 211–212, 317–331. doi: 10.1016/j.jhazmat.2011.10.016

Huijgen, W. J. J., and Comans, R. N. J. (2005). Mineral CO₂ sequestration by steel slag carbonation. *Environ. Sci. Technol.* 39, 9676–9682. doi: 10.1021/es050795f

Iida, H., Takayanagi, K., Nakanishi, T., and Osaka, T. (2007). Synthesis of Fe₃O₄ nanoparticles with various sizes and magnetic properties by controlled hydrolysis. *J. Colloid Interf. Sci.* 314, 274–280. doi: 10.1016/j.jcis.2007.05.047

Atlas Iron Company (2009). *Ridley Magnetite Project - Preliminary Feasibility Study Outcomes*. West Perth: Atlas Iron Company.

Kakizawa, M., Yamasaki, A., and Yanagisawa, Y. (2001). A new CO2 disposal process via artificial weathering of calcium silicate accelerated by acetic acid. *Energy* 26, 341–354. doi: 10.1016/S0360-5442(01)00005-6

Kelland, D. R. (1998). Magnetic separation of nanoparticles. *IEEE Trans. Magn.* 34, 2123–2125. doi: 10.1109/20.706824

Kelland, D. R., Maxwell, E., and Oberteuffer, J. (1975). *High Gradient Type Magnetic Separator with Continuously Moving Matrix*. Patent No. US3902994 A.

Kim, E. H., Lee, H. S., Kwak, B. K., and Kim, B.-K. (2005). Synthesis of ferrofluid with magnetic nanoparticles by sonochemical method for MRI contrast agent. *J. Magn. Magn. Mater.* 289, 328–330. doi: 10.1016/j.jmmm.2004.11.093

Legodi, M., and Dewaal, D. (2007). The preparation of magnetite, goethite, hematite and maghemite of pigment quality from mill scale iron waste. *Dyes Pigments* 74, 161–168. doi: 10.1016/j.dyepig.2006.01.038

Lorente, E., Herguido, J., and Pea, J. A. (2011). Steam-iron process: influence of steam on the kinetics of iron oxide reduction. *Int. J. Hydrog. Energy* 36, 13425–13434. doi: 10.1016/j.ijhydene.2011.07.111

Malvoisin, B., Brunet, F., Carlut, J., Montes-Hernandez, G., Findling, N., Lanson, M., et al. (2013). High-purity hydrogen gas from the reaction between BOF steel slag and water in the 473–673 K range. *Int. J. Hydrog. Energy* 38, 7382–7393. doi: 10.1016/j.ijhydene.2013.03.163

Malvoisin, B., Carlut, J., Brunet, F. (2012). Serpentinization of oceanic peridotites: 1. A high-sensitivity method to monitor magnetite production in hydrothermal experiments. *J. Geophys. Res.* 117:B01104. doi: 10.1029/2011JB008612

Marcaillou, C., Muñoz, M., Vidal, O., Parra, T., and Harfouche, M. (2011). Mineralogical evidence for H2 degassing during serpentinization at 300°C/300bar. *Earth Planet. Sci. Lett.* 303, 281–290. doi: 10.1016/j.epsl.2011.01.006

Morawski, A. M., Lanza, G. A., and Wickline, S. A. (2005). Targeted contrast agents for magnetic resonance imaging and ultrasound. *Curr. Opin. Biotechnol.* 16, 89–92. doi: 10.1016/j.copbio.2004.11.001

Mornet, S., Vasseur, S., Grasset, F., and Duguet, E. (2004). Magnetic nanoparticle design for medical diagnosis and therapy. *J. Mater. Chem.* 14:2161. doi: 10.1039/b402025a

Munoz, M., de Pedro, Z. M., Casas, J. A., and Rodriguez, J. J. (2015). Preparation of magnetite-based catalysts and their application in heterogeneous Fenton oxidation – a review. *Appl. Catal. B Environ.* 176–177, 249–265. doi: 10.1016/j.apcatb.2015.04.003

Oberteuffer, J. (1973). High gradient magnetic separation. *IEEE Trans. Magn.* 9, 303–306. doi: 10.1109/TMAG.1973.1067673

Patel, R. D., Hopper, M. A., Bartel, J., and Zwartz, E. G. (2003). *Magnetite Toner Processes*. Patent No. US20030180649 A1.

Piatak, N. M., Parsons, M. B., and Seal, R. R. (2015). Characteristics and environmental aspects of slag: a review. *Appl. Geochem.* 57, 236–266. doi: 10.1016/j.apgeochem.2014.04.009

Raj, K., and Moskowitz, B. (1990). Commercial applications of ferrofluids. *J. Magn. Magn. Mater.* 85, 233–245. doi: 10.1016/0304-8853(90)90058-X

Raj, K., Moskowitz, B., and Casciari, R. (1995). Advances in ferrofluid technology. *J. Magn. Magn. Mater.* 149, 174–180. doi: 10.1016/0304-8853(95)00365-7

Sacripante, G. G., and Kmiecik-Lawrynowicz, G. E. (1994). *Toner Processes*. Patent No. US5308734 A.

Stumm, W. (1997). Reactivity at the mineral-water interface: dissolution and inhibition. *Colloids Surf. Physicochem. Eng. Asp.* 120, 143–166. doi: 10.1016/S0927-7757(96)03866-6

Sun, S., and Zeng, H. (2002). Size-controlled synthesis of magnetite nanoparticles. *J. Am. Chem. Soc.* 124, 8204–8205. doi: 10.1021/ja026501x

Taut, T., Kleeber, R., and Bergmann, J. (1998). The new Seifert Rietveld program BMGN and its application to quantitative phase analysis. *Mater. Struc.* 5, 57–66.

Teir, S., Eloneva, S., Fogelholm, C.-J., and Zevenhoven, R. (2007). Dissolution of steelmaking slags in acetic acid for precipitated calcium carbonate production. *Energy* 32, 528–539. doi: 10.1016/j.energy.2006.06.023

Teir, S., Eloneva, S., Revitzer, H., Zevenhoven, R., Salminen, J., Fogelholm, C.-J., et al. (2011). *Method of Producing Calcium Carbonate from Waste and by-Products*. Patent No. US20110139628 A1.

Tiefenauer, L. X., Tschirky, A., Kühne, G., and Andres, R. Y. (1996). *In vivo* evaluation of magnetite nanoparticles for use as a tumor contrast agent in MRI. *Magn. Reson. Imaging* 14, 391–402. doi: 10.1016/0730-725X(95)02106-4

van Oss, H. G. (2013). Slag, iron and steel. *Miner. Yearb. 2011.* Reston, VA: U.S. Geological Survey.

World Steel Association (2015). *Steel Statistical Yearbook 2015.* Brussels: Worldsteel Committee on Economic Studies

Xu, P., Zeng, G. M., Huang, D. L., Feng, C. L., Hu, S., Zhao, M. H., et al. (2012). Use of iron oxide nanomaterials in wastewater treatment: a review. *Sci. Total Environ.* 424, 1–10. doi: 10.1016/j.scitotenv.2012.02.023